



# High-Temperature Oxidation and Smelt Deposit Corrosion of Ni-Cr-Ti Arc-Sprayed Coatings

S. Matthews and M. Schweizer

(Submitted November 22, 2012; in revised form March 17, 2013)

High Cr content Ni-Cr-Ti arc-sprayed coatings have been extensively applied to mitigate corrosion in black liquor recovery boilers in the pulp and paper industry. In a previous article, the effects of key spray parameters on the coating's microstructure and its composition were investigated. Three coating microstructures were selected from that previous study to produce a dense, oxidized coating (coating A), a porous, low oxide content coating (coating B), and an optimized coating (coating C) for corrosion testing. Isothermal oxidation trials were performed in air at 550 and 900 °C for 30 days. Additional trials were performed under industrial smelt deposits at 400 and 800 °C for 30 days. The effect of the variation in coating microstructure on the oxidation and smelt's corrosion response was investigated through the characterization of the surface corrosion products, and the internal coating microstructural developments with time at high temperature. The effect of long-term, high-temperature exposure on the interaction between the coating and substrate was characterized, and the mechanism of interdiffusion was discussed.

**Keywords** arc-sprayed microstructure, black liquor recovery boiler, high-temperature oxidation, Ni-Cr-Ti, smelt deposit corrosion

## 1. Introduction

High Cr content Ni-Cr-Ti arc-sprayed coatings have been extensively applied to mitigate corrosion in black liquor recovery boilers in the pulp and paper industry (Ref 1, 2). In a previous article (Ref 3), the effects of key spray parameters on the coating microstructure were investigated in the statistical optimization of arc-sprayed Ni-Cr-Ti coatings. In that cited study, it was highlighted that a broad range of coating microstructures were generated under representative industrial spray parameters—oxide content varied from 9 to 29 vol.%, porosity from 5 to 9 vol.%, and splat thickness from 11 to 35  $\mu\text{m}$ . Previous studies have highlighted that the coating microstructure plays a dominant role in the corrosion of thermal spray coatings, with corrosive species preferentially penetrating into the coating along splat boundaries and through pockets of porosity (Ref 4-6). The morphology of

the splats and their average thickness contribute toward the coating's "free path to substrate", a term defined by Bluni and Marder (Ref 4) to characterize the distance from the coating surface to the substrate via continuous diffusion paths formed by splat boundaries and pores. Coatings with longer "free path to substrate" distances have been shown to provide superior corrosion resistance for a given exposure environment (Ref 4). The coating's feedstock composition is also a determining factor in the coating's corrosion resistance (Ref 5, 6). A complicating factor is that the coating composition can change dramatically from the engineered composition of the feedstock material because of in-flight oxidation. This is of critical concern for this coating composition in black liquor recovery boilers, where its success has been attributed to the ability of the high Cr content to enable oxidation within the coating to seal off the splat boundaries and prevent sulfur penetration into the coating (Ref 2).

The aim of this study was to assess what effect the variation in coating microstructure had on the corrosion performance. The reducing and sulfidizing atmosphere within black liquor recovery boilers generates extremely complex corrosion responses, even for bulk wrought alloys (Ref 7-9). As a first step in this investigation, a simplified oxidation-only study was performed at low (550 °C) and high (900 °C) temperatures in air. The low-temperature trial was selected to investigate the effect of coating porosity on the extent of internal oxidation, while the high-temperature trial was intended to highlight the effect of Cr loss during spraying on the oxidation response. These results were contrasted to trials in argon under industrial smelt deposits at 400 and 800 °C. The latter trials did not have the reducing/sulfidizing gaseous atmosphere typical of industrial black liquor recovery boilers,

S. Matthews, School of Engineering and Advanced Technology, Massey University, Private Bag 102904, Auckland 0745, New Zealand; M. Schweizer, Department of Chemical and Materials Engineering, The University of Auckland, Private Bag 92019, Auckland Mail Centre, Auckland 1142, New Zealand; and Department of Surface and Materials Technology, Aalen University of Applied Sciences, Beethovenstraße 1, 73430 Aalen, Germany. Contact e-mail: s.matthews@massey.ac.nz.

**Table 1** Summary of the spray parameters and coating properties for coatings A, B, and C

	Coating A“Oxidized coating”	Coating B“Porous coating”	Coating C“Optimized coating”
Current, A	250	150	250
Voltage, V	25	25	25
Atomizing air pressure, bar	4.2	3	3
Spray distance, mm	200	200	150
Spray passes	10	20	10
Porosity, vol. %	3.6	5.3	3.5
Oxide content, vol. %	28.4	18.5	18.7
Microhardness, VHM <sub>300</sub>	389	339	321
Coating thickness, $\mu\text{m}$	460	494	436

and so were focused on corrosion induced by the smelt layer alone. The lower temperature was selected to simulate the operating temperature of coated water-wall tubes in the lower furnace area (Ref 10). The higher temperature is greater than the melting point of smelt (Ref 11) and was selected to simulate corrosion of coatings on components operating under molten smelt or prone to splashing of molten smelt. Three coatings were tested in each trial—a dense but heavily oxidized coating, a porous coating, and a coating with an “optimized” microstructure based on the previous statistical optimization trials.

## 2. Experimental Procedure

### 2.1 Arc-Spray Sample Preparation

All coatings were sprayed with an industrial arc-spray system (Metallisation Arc-spray 234 Gun connected to a Metallisation Series V 300 Energizer) using 1.6-mm diameter wires of nominal composition Ni-43Cr-0.3Ti (Praxair-Tafa 45CT wire). Coatings were sprayed onto degreased and gritblasted substrates of  $60 \times 60 \times 3 \text{ mm}^3$  304 stainless steel and  $60 \times 60 \times 5 \text{ mm}^3$  boiler plate steel (Carbon-Manganese steel for boiler applications—Specification AS1548-7-460R). Coatings were sprayed with sufficient passes to generate a nominal coating thickness of 500  $\mu\text{m}$ . An additional set of 304 stainless steel substrates were prepared and sprayed on both sides, with a nominal coating thickness of 250  $\mu\text{m}$  on each side. The arc-spray gun was mounted on a six-axis robot that moved the gun in a horizontal raster pattern from the top to the bottom, with a 10-mm drop between each horizontal traverse. The traverse speed was 500 mm/s. Three spray parameters settings were selected from Ref 3 to generate a dense, oxidized structure (coating A), a low oxide content, porous coating microstructure (coating B), and a dense, low oxide content-optimized coating microstructure (coating C), Table 1.

### 2.2 As-Sprayed Coating Characterization

The as-sprayed samples were sectioned using a metallographic cutoff machine and mounted in epoxy using vacuum impregnation. All of the mounts were metallographically ground and polished at the same time using a

multiple sample holder in a semiautomated grinder polisher to prevent sample to sample variation during preparation. The coatings' cross sections were characterized by optical microscopy and image analysis using ImageJ (Ref 12) to measure the volume fraction of porosity and oxide, and the coating's thickness. The Vickers microhardness was measured under a 300-g load for 10 s (LECO M-400 hardness tester, LECO, USA). The wire and coatings' phase distributions were characterized on cross-sectional samples using scanning electron microscopy (SEM) [with backscattered electron (BSE) imaging] (FEI Quanta F, USA) and energy dispersive spectroscopy (EDS, EDAX, USA). EDS analysis was carried out for elements of atomic mass greater than Na because of the poor accuracy in quantifying lighter atomic mass elements. X-ray diffraction (Bruker D2 Phaser, Cu source at 30 kV and 10 mA, Bruker AXS, Germany) was used in conventionally locked couple mode to determine the composition of the wire and coatings. Before quantitative analysis of the XRD patterns, the contribution of  $K\alpha_2$  radiation was stripped from the pattern, and the background was removed using the instrument software.

### 2.3 Oxidation Trials

Oxidation trials in still air were carried out at 550 and 900 °C in box furnaces using the 304 stainless steel substrate samples. Samples of  $15 \times 15 \text{ mm}^2$  were cut from the larger plates for testing. The oxidative mass gain was measured at each temperature using substrates coated on both sides. A sample from each coating was removed after 5, 15, and 30 days of exposure and weighed. The coating composition was analyzed after each exposure time using XRD in conventionally locked couple mode and in the more surface sensitive glancing angle mode (Bruker D8 Advance, glancing angle 6°, Cu source at 40 kV and 40 mA, Bruker AXS, Germany). SEM and EDS analysis was performed on the oxidized coating cross sections for all exposure times for coating C, and for the 30-day exposure times for coatings A and B. The bulk coating elemental composition was measured by EDS using full screen area scans at a magnification of 1000 $\times$ , for a minimum of three images per sample. The variation in splat to splat composition was measured using EDS spot scans in individual surface splat cross sections on a minimum of five splats per sample. EDS line scans from the substrate into the coating were used to measure the distribution of

the main substrate and coating elements. The variation in internal oxidation with time was assessed by image analysis of the coating cross sections at a magnification of  $500\times$ . Each image was digitally cut into strips with the width of the image and a height of  $47\ \mu\text{m}$ . The first strip was taken at the coating surface below the oxide layer. Successive strips were taken below this for a total of six strips per image. Image analysis was used to characterize the volume percent of oxide per strip based on the measured oxide area fraction. Three images per sample were processed in this way, and the results were averaged. SEM was also used to image the oxidized surface topography of coating C samples after each exposure period at both temperatures.

## 2.4 Smelt Deposit Corrosion

Smelt from an industrial black liquor recovery boiler was used for the smelt deposit trials. The smelt was ground to a fine powder using a mortar and pestle. The composition and structure of the powder was characterized using XRD, SEM and EDS. To apply the smelt to the coating samples the smelt powder was mixed with ethanol to form a paste and applied to the top of the coatings. The low-temperature smelt trials used the arc-sprayed boiler plate steel substrate samples to simulate the industrial coating system, while the high-temperature smelt trials used the arc-sprayed stainless steel substrate samples. For the  $400\ ^\circ\text{C}$  trials, the smelt-coated samples were placed in the cup-shaped Schedule 40 mild steel end caps and covered with a thick layer of activated carbon powder, Fig. 1. Three steel end caps were used to allow the samples to be removed after 5, 15, and 30 days. The steel end caps were placed inside an Inconel canister suspended within a vertical furnace and sealed. Argon gas was used to flood the sample chamber and then fed continuously at a slow nominal flowrate during testing. The carbon powder and argon gas purging were used to minimize oxidation of the samples during testing. For the  $800\ ^\circ\text{C}$  trials, the smelt-covered samples were supported on a ceramic holder within a horizontal tube furnace. The ends of the tube were sealed and the tube flooded with argon to minimize the exposure to oxygen during testing. Samples were removed after 5, 15, and 30 days. After testing, the smelt material was scrapped off, and the coating surface gently was cleaned with a nylon brush to remove any loose material. The topographical composition was assessed by XRD. Cross-sectional samples were metallographically prepared and analyzed by SEM and EDS for all coatings treated for 30 days at both temperatures.

## 3. Results and Discussion

### 3.1 As-Sprayed Coating Characterization

The three coatings used in these trials have been previously characterized in detail in Ref 3. A brief summary of the key coating attributes is presented in this article as a basis of comparison for the oxidized samples. Coating A

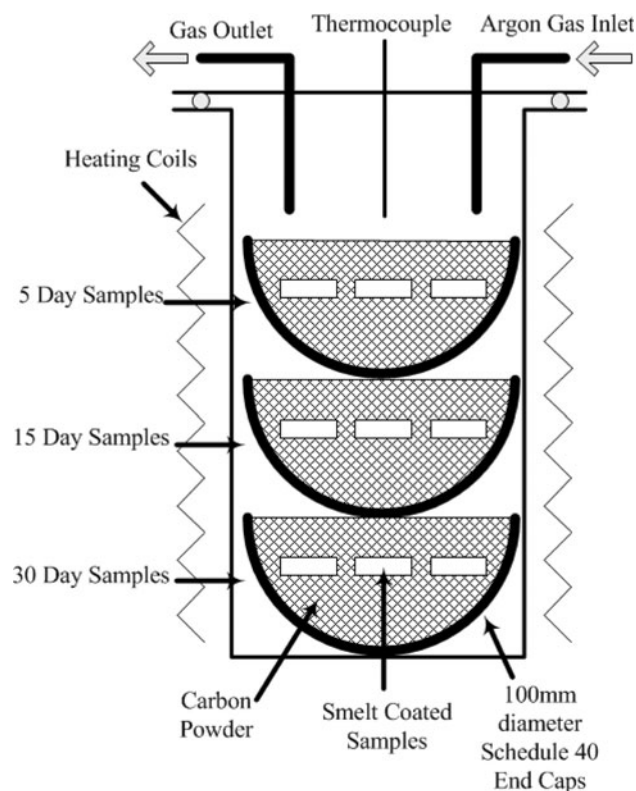


**Fig. 1** Schematic of the sample set up in the vertical furnace for the  $400\ ^\circ\text{C}$  smelt trials

exhibited a typical arc-sprayed microstructure incorporating a broad distribution of well-molten splats (bright contrast phase) with a high concentration of oxide stringers (dark gray contrast phase), Fig. 2 and Table 1. The high oxide content is thought to be the primary factor in this coating having the highest microhardness ( $389\ \text{VHN}_{300}$ ), Table 1, which exceeded that of the starting wire ( $330\ \text{VHN}_{300}$ ) (Ref 3). Coating B had a larger and more blocky splat morphology which led to a higher level of porosity (5.3 vol.%). However, the oxide content was significantly lower than in coating A, Table 1. Coating C had a structure intermediate between the previous coatings, exhibiting a dense structure of well-molten splats with a low oxide content, Fig. 2 and Table 1.

The XRD patterns of all the coatings were dominated by the same Ni alloy peaks as seen in the starting wire with subtle differences (Ref 3). These peaks formed a higher  $2\theta$  “tail” which was indicative of a variation in the Ni alloy composition during spraying. The main Ni peak was also overlapped by a higher  $2\theta$  peak attributed to the precipitation of the equilibrium Cr-rich second phase predicted from the Ni-Cr-Ti phase diagram (Ref 13). Coating A showed the most significant development of the  $2\theta$  “tail” and Cr phase, Fig. 3(a), with such features of lower intensity in coatings B and C.  $\text{Cr}_2\text{O}_3$  was the only oxide phase observed and was most apparent in coating A. The composition of this oxide was complicated by the elevated concentrations of Ti observed in the EDS analysis, suggesting the formation of a mixed (Cr,Ti) $_2\text{O}_3$  oxide composition.

Spraying did not result in a significant loss of any alloy elements, but it did lead to a significant redistribution of the elements into different phases. In-flight oxidation effectively stripped the reactive elements Ti and Al from the alloy to leave the splats as Ni-Cr alloys. Oxide formation also reduced the alloy phase Cr content in the surface splats from 43 wt.% Cr in the wire to 34 wt.% Cr in coating A and 40-41 wt.% Cr in coatings B and C.

### 3.2 Oxidation Trials

**3.2.1 Mass Gain: 550 and 900 °C Oxidation.** At 550 °C, the coatings showed significant mass gains over the first 5 days, beyond which the rate of mass gain decreased up to 30 days, Fig. 4. Coating C showed the lowest mass gain, while coating B had the highest. At 900 °C, the mass gain at 5 days was significantly higher than that at 550 °C. However, the rate of mass gain over the remaining 25 days was comparable to that at 550 °C in spite of the higher oxidation rate (NB: the 5-day result for coating C is believed to be an anomalous result generated by a defective or damaged sample). Coatings A and C showed comparable mass gains, while coating B was distinctly higher. This suggests that the porous microstructure in coating B played a more significant role in the mass gain response, compared to the effect of Cr reduction by in-flight oxidation in coating A.

**3.2.2 Topographical Analysis: 550 °C Oxidation.** Significant oxide growth occurred after 5 days at 550 °C on coating A in the conventionally locked couple mode XRD analysis, Fig. 3.  $\text{Cr}_2\text{O}_3$  dominated the oxide composition. However, additional analysis using glancing angle XRD indicated that NiO (JCPDS 47-1049) and  $\text{NiCr}_2\text{O}_4$  (JCPDS 23-1271) had also formed at this time. The Ni phase remained preferentially oriented but had undergone a degree of compositional refinement, with the higher 2 $\theta$  tail and neighboring Cr peak being more definitive relative to the as-sprayed coating. The oxide peaks in coating B and C were comparable and of a lower intensity for Ni compared with coating A, indicative of lower oxide formation.  $\text{Cr}_2\text{O}_3$  was the only oxide observed in both the locked couple and glancing angle XRD patterns.

After 15 days, NiO and  $\text{NiCr}_2\text{O}_4$  were observed on all three coatings, in addition to significant growth of  $\text{Cr}_2\text{O}_3$ . The Ni alloy transformation was apparent in all coatings, which showed comparable broadening of the Ni peaks and development of the Cr peak. The Ni oxide peaks continued to develop in coating A up to 30 days, particularly the NiO peaks.  $\text{NiCr}_2\text{O}_4$  was the only Ni oxide seen after 30 days in coatings B and C. This implies that a continuous  $\text{Cr}_2\text{O}_3$  layer had formed, preventing development of any Ni oxides and leading to the reaction of NiO and  $\text{Cr}_2\text{O}_3$  to form the spinel phase. Quantification of the  $\text{Cr}_2\text{O}_3/\text{Ni}$  peak area ratios showed that coating A had a consistently higher oxide concentration across all exposure times relative to the other coatings. This trend, in combination with the limited Ni oxide development, results from the higher retained Cr concentration in coatings B and C which enabled protective  $\text{Cr}_2\text{O}_3$  layers

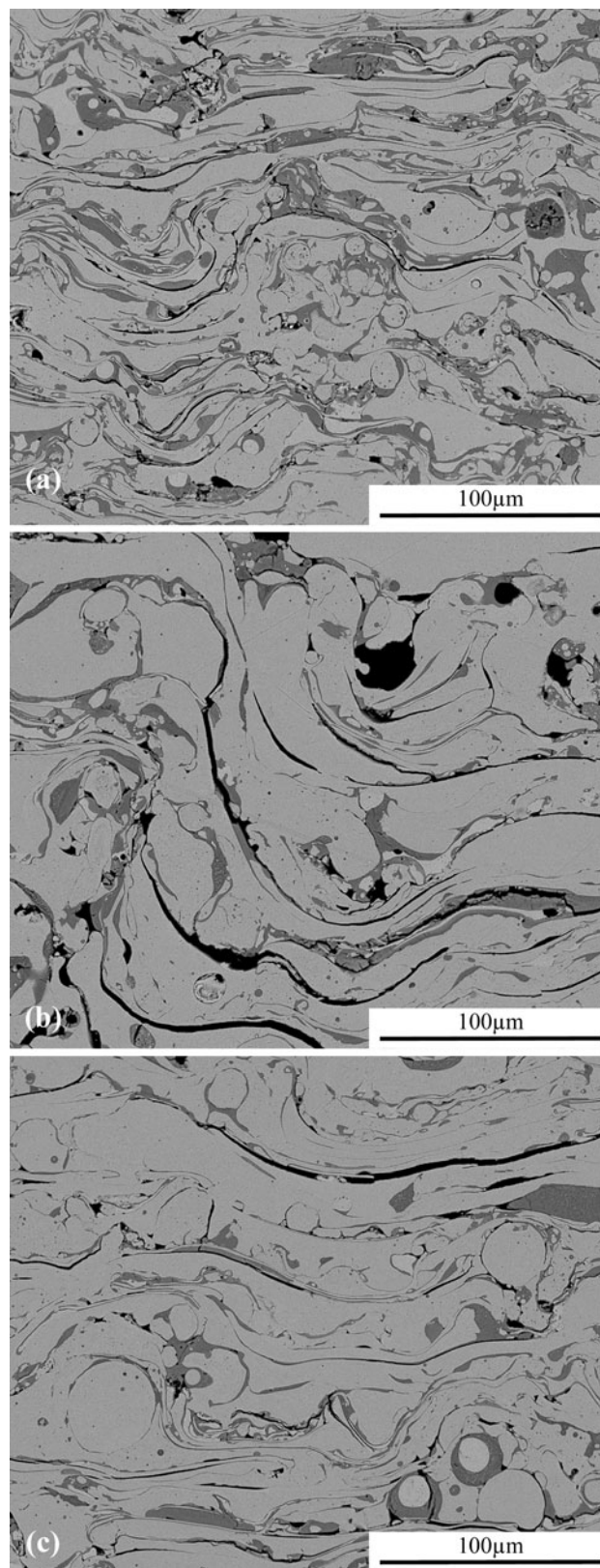


**Fig. 2** Cross-sectional BSE images of the as-sprayed coatings—coating A (a), coating B (b), and coating C (c)

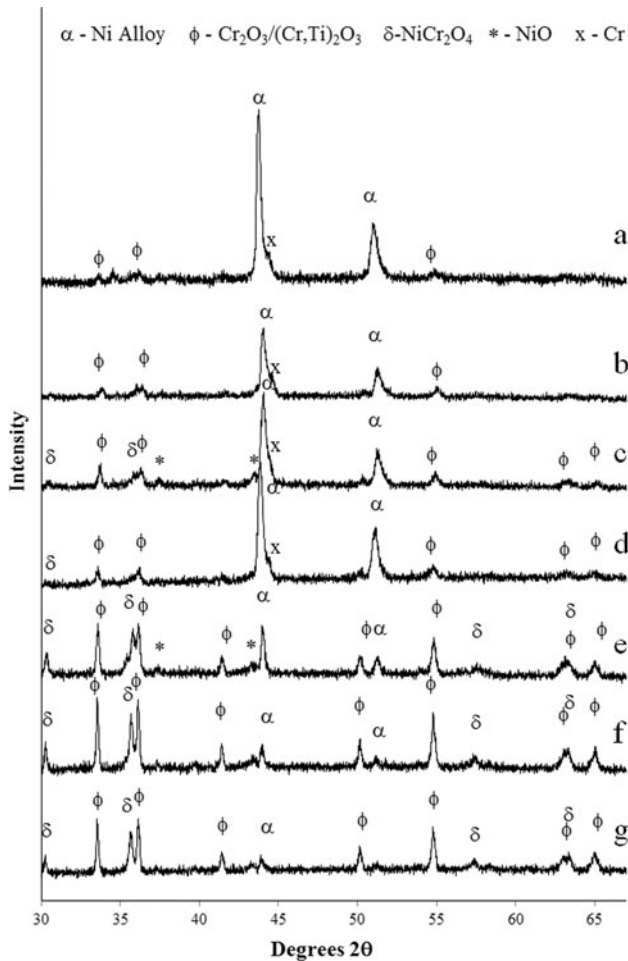


**Fig. 3** XRD patterns—coating A as-sprayed (a). Oxidation at 550 °C—coating A after 5 days (b) and 30 days (c) and coating C after 30 days (d). Oxidation at 900 °C—coating A after 5 days (e) and 30 days (f) and coating C after 30 days (g)

to develop before significant Ni oxide growth could occur (Ref 7).

The topographical development of the surface oxide with time on coating C is shown in Fig. 5. The as-sprayed coating showed a heterogeneous mixture of splat morphologies, ranging from small spherical particles through to large flat disk splats, Fig. 5(a). The splat surfaces were typically smooth with only thin oxide layers observed. The variation in Cr concentration in the splats led to a heterogeneous oxide layer development after 5 days, Fig. 5(b). The large flat splats remained very smooth with minimal oxide growth, while significant Ni oxide development was apparent on the smaller, more distorted splats. This heterogeneous oxide development continued up to 30 days, Fig. 5(c). While oxide layers were evident on all the splats at this time, the size of the oxide features and thickness of the oxide layer appeared very small relative to the splat morphology. It was not obvious from these images that the oxide layers developed would be sufficient to seal up the porosity and splat boundaries within the coating. This is significant because the mass gain kinetics indicated a slow

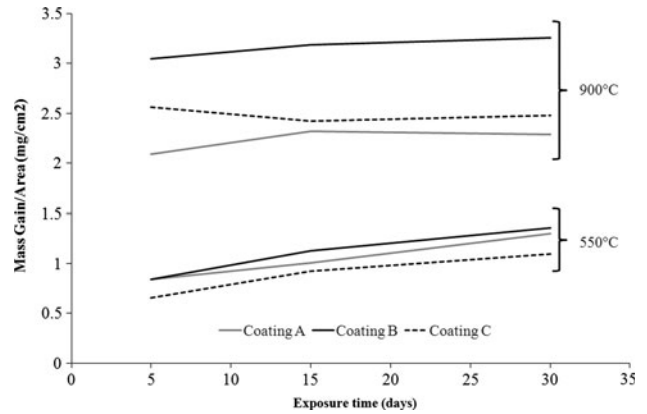


**Fig. 4** Mass gain/area results for the three coatings at 550 and 900 °C

rate of oxide growth at this time, implying that the oxide structure would not change significantly from that seen at 30 days. If oxide development was not sufficient to seal the coating by this time, then corrosive species would still be able to diffuse into the coating along splat boundaries. As such, the splat size and morphology, and the overall coating thickness would play a critical role in the corrosion resistance of the coating at the temperature because of their effect on determining the “free path to substrate” (Ref 4).

**3.2.3 Cross-Sectional Analysis: 550 °C Oxidation.** After 5 days at 550 °C, the splat boundaries and pockets of porosity in coating C became more distinct relative to the as-sprayed coating because of internal oxidation, Fig. 6(a). Within the splats, the equilibrium Cr-rich second phase had precipitated as small mid-gray contrast features that were darker than the alloy but brighter than the oxide. The Cr-rich precipitates continued to develop in concentration and increased in size up to 30 days, Fig. 6(b) and (c). Minimal refinement of the splat structure or oxide morphology occurred over this time with the coating morphology very similar to the as-sprayed coating. There was no sign of splat sintering or break up/spheroidization of the oxides. The microstructural developments of coating A and B after 30 days closely resembled those in coating C. The only significant difference appeared to be the lower concentration of Cr-rich precipitates that formed in coating A, due to the lower retained Cr content, compared with coatings B and C. This observation is contrary to the XRD results where the Cr peak was more distinct in coating A than in the other coatings. Further study is required to resolve this variation. In all cases, the coatings were protective of the substrate, with no obvious oxide formation at the coating/substrate interface after 30 days.

The subtle development of internal oxide was quantified in the analysis of coating cross section “strips” as a function of depth. In the as-sprayed condition, coating C had an average oxide volume formation of 15-16 vol.% that was consistent through the depth of analysis, Fig. 7(a). These oxide content values were slightly less than that measured in the initial bulk cross-sectional

characterization of the coatings presented in Table 1. With the increasing oxidation time, the oxide concentration increased, reaching an average level of 21-22 vol.% after 30 days. This oxide content was also consistent over the depth of analysis, indicating that internal oxidation had occurred to a depth of more than 250  $\mu\text{m}$ . This highlights the critical importance of the coating thickness in providing a sufficient barrier to the penetration of corrosive gases to the substrate. While it may seem obvious to simply increase the coating thickness to improve the corrosion resistance, issues regarding residual stress and substrate-coating thermal expansion variations increase with increasing thickness, as does the cost of application. Furthermore, it reinforces the importance of quantifying the actual coating thickness independent of surface roughness effects (Ref 3). After 30 days, coating B showed a result comparable with coatings C, while coating A was distinctly higher, Fig. 7(b). However, the oxide content in coating A was high to begin with (approximately 27 vol.% in the as-sprayed coating), and so the increase in the internal oxide content was negligible compared with the two other coatings. EDS scans in the surface splats showed no significant change in the splat's composition upon oxidation after 30 days, in spite of internal oxidation.

**3.2.4 Topographical Analysis: 900 °C Oxidation.** After 5 days at 900 °C, the  $\text{Cr}_2\text{O}_3$  peaks in the XRD pattern of coating A were of higher intensity than the Ni alloy peaks as shown in Fig. 3(e). While  $\text{Cr}_2\text{O}_3$  dominated the oxide composition, both NiO and  $\text{NiCr}_2\text{O}_4$  were also present in the locked couple XRD pattern. No NiO peaks were seen in coatings B and C but  $\text{NiCr}_2\text{O}_4$  peaks were well established. However, the intensities of the  $\text{NiCr}_2\text{O}_4$  peaks relative to the  $\text{Cr}_2\text{O}_3$  peaks were distinctly lower than in coating A. This is reflective of the higher Cr content of these coatings which enabled a continuous  $\text{Cr}_2\text{O}_3$  layer to form faster than on coating A, which minimized NiO formation and subsequent  $\text{NiCr}_2\text{O}_4$  formation. In all the coatings, the main Ni peak was symmetric with no obvious higher 2 $\theta$  tail and no obvious Cr peak. While a reduction in the alloy Cr content due to oxidation is a contributing factor in this, the low concentration of Cr within the analyzed volume and lower intensity of the Ni alloy peaks due to surface oxide formation are the most likely reasons for the lack of a distinct Cr peak.

After 15 days, NiO was no longer observed in the XRD pattern of coating A, with this phase having reacted with  $\text{Cr}_2\text{O}_3$  to form  $\text{NiCr}_2\text{O}_4$ . Continued oxide growth up to 30 days meant that the oxide phase peaks dominated over those of the Ni alloy in all coatings, with only low concentrations of  $\text{NiCr}_2\text{O}_4$  having been left behind from earlier exposure times. Peak area analysis highlighted that coating A had the highest concentration of  $\text{Cr}_2\text{O}_3$  at each exposure time, but the difference between this and the other coatings was significantly reduced relative to the results at 550 °C. The main difference between the coatings was the significantly greater amount of Ni oxides that formed on coating A relative to coatings B and C with short-term exposure. NiO was present in the XRD pattern of coating A after 5 days but was not seen in the patterns

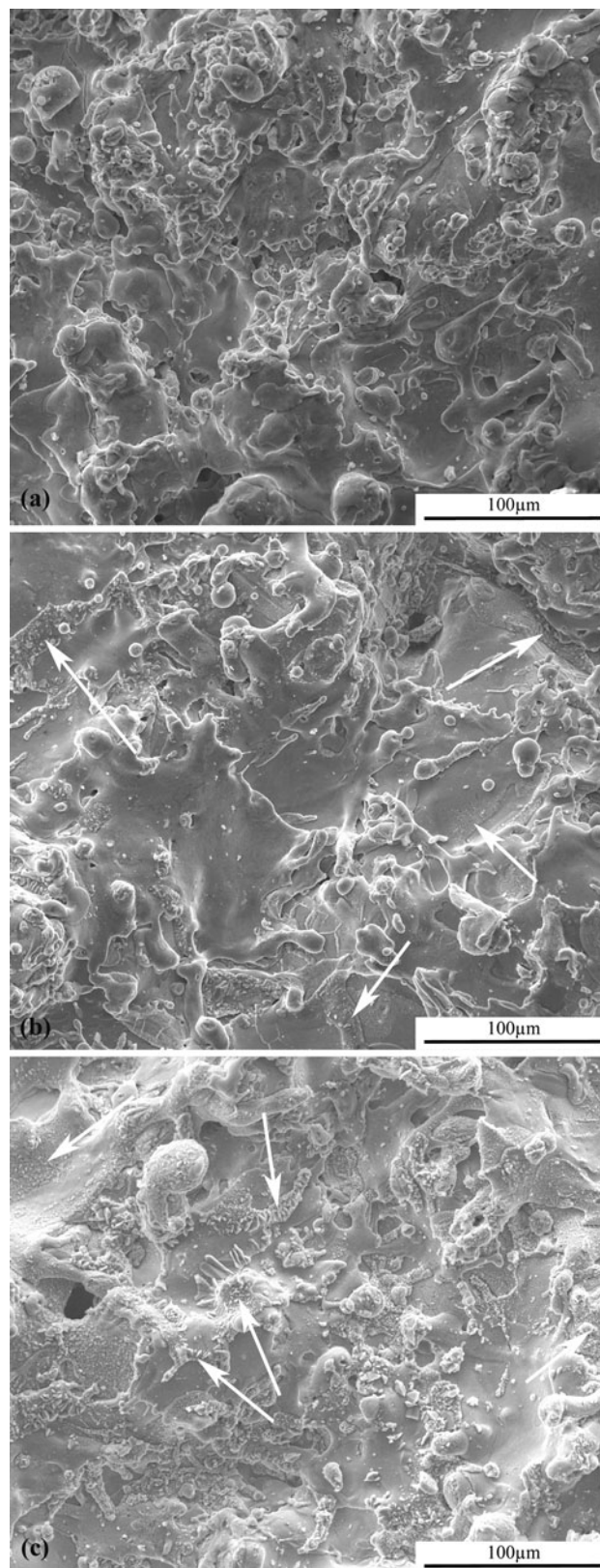


**Fig. 5** Topographical SEM images of coating C—as-sprayed condition (a) and after 5 days (b) and 30 days (c) at 550 °C. The white arrows highlight regions of oxide formation on the splat surfaces

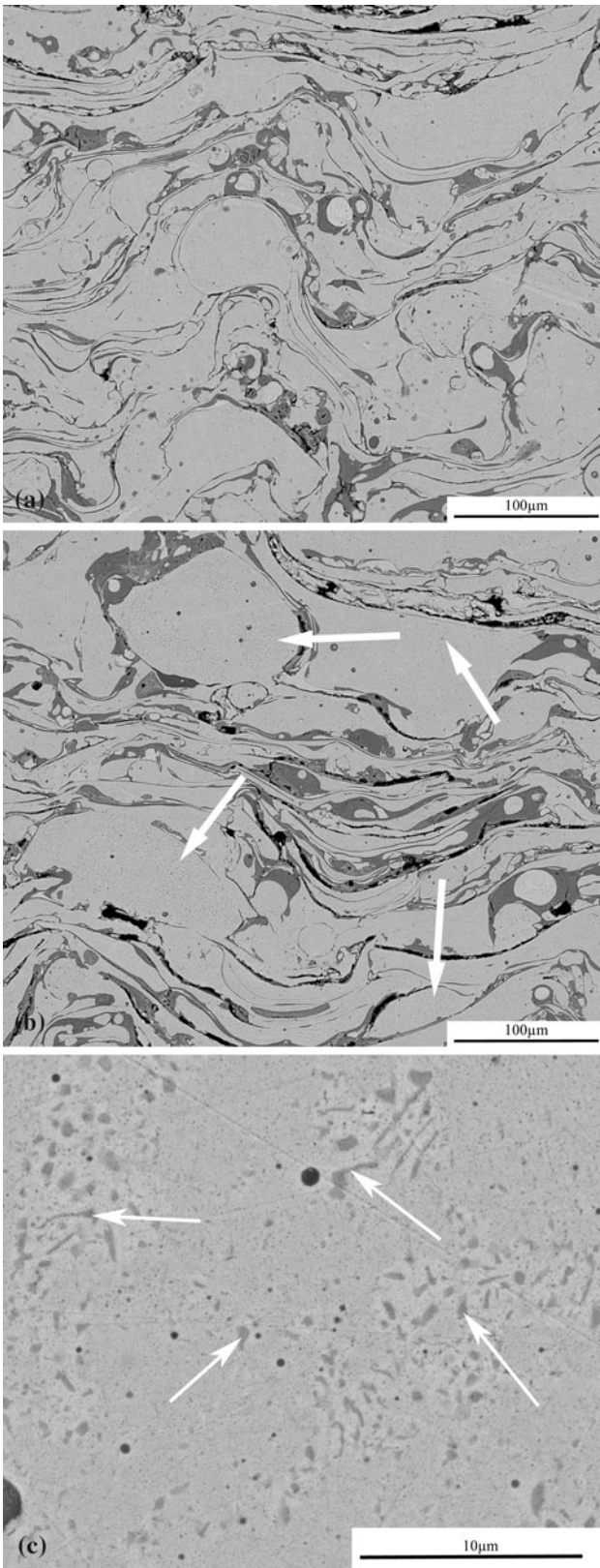


**Fig. 6** Cross-sectional BSE images of coating C after 5 days (a) and 30 days (b) at 550 °C. Higher magnification image of the Cr-rich precipitates formed after 30 days in coating C (c). The arrows highlight the presence of the fine Cr-rich second phase precipitates

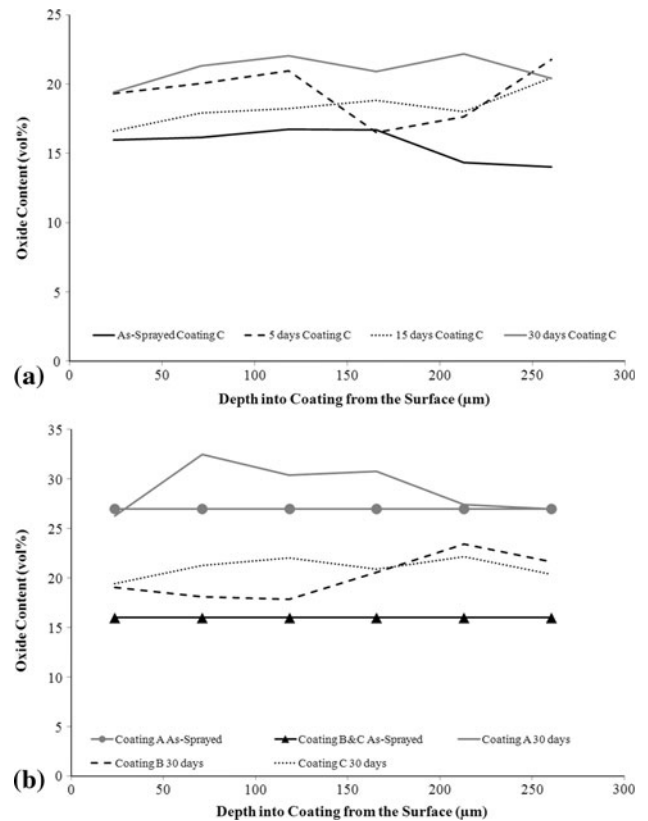


**Fig. 7** “Strip” analysis of the internal oxide content for coating C—as-sprayed condition and after 5, 15, and 30 days at 550 °C (a), and for the all of the coatings after 30 days at 550 °C (b)

of coating B and C. Similarly, the peaks from  $\text{NiCr}_2\text{O}_4$  were more definitive in coating A at this early exposure time. However, after 30 days, the extent of  $\text{NiCr}_2\text{O}_4$  formation relative to the other oxide phases was comparable in all three coatings.

A continuous oxide layer had developed on all of the splats of coating C after 5 days, with only minor variations in oxide grain size and morphology, Fig. 8(a). The oxide thickness was sufficient to obscure the underlying splat morphology such that only the largest splats were observable. Figure 9 shows a cross-sectional image of the oxide layer formed after 5 days at 900 °C on coating C. A  $\text{NiCr}_2\text{O}_4$  layer can be seen above a well-developed  $\text{Cr}_2\text{O}_3$  layer, which prevents any further Ni oxide development. The thickness of this oxide layer is sufficient to overshadow the surface profile generated by the splat’s structure, which indicates that the splat boundaries had become sealed by internal oxidation at this time. Extended exposure up to 30 days led to growth in the oxide grain size, but no significant changes were observed in oxide morphology, Fig. 8(b).

**3.2.5 Cross-Sectional Analysis: 900 °C Oxidation.** Significant intersplat sintering occurred within the first 5 days of testing at 900 °C in coating C, Fig. 10(a). The original splat structure was evident only by the morphology of the oxide stringers. The thin oxide layers had begun to break up from plate-like intersplat oxides into multiple discrete

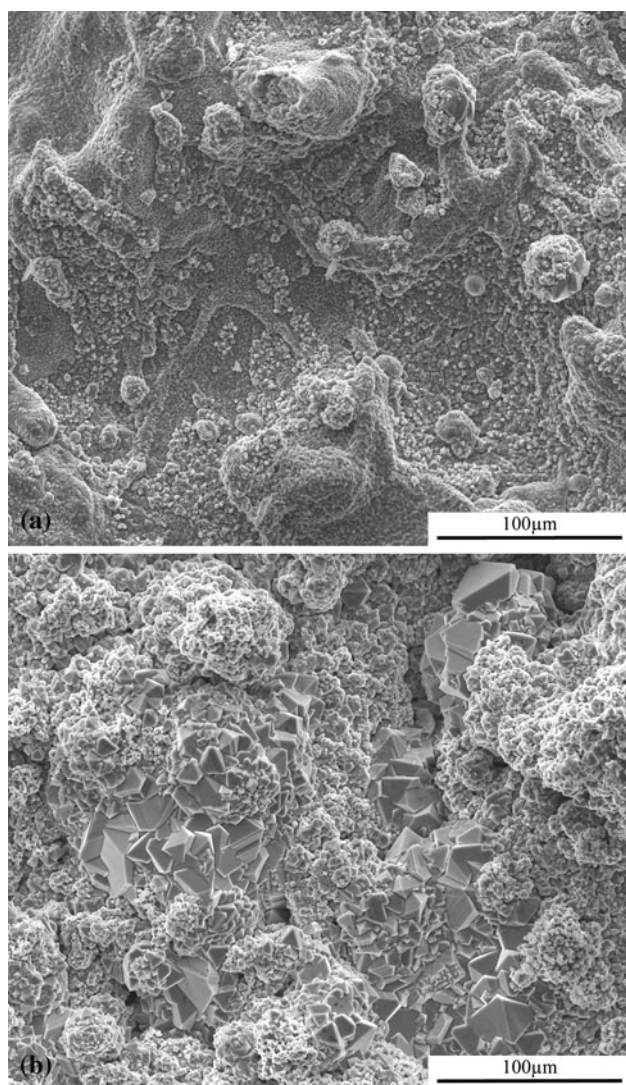
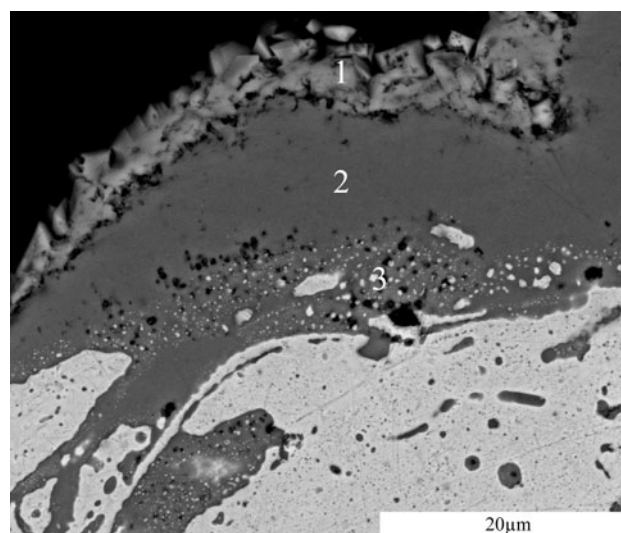


**Fig. 8** Topographical SEM images of coating C after 5 days (a) and 30 days (b) at 900 °C

spherical features. The coating had essentially sintered together into a bulk continuous layer. Any internal oxidation must therefore have occurred within the first 5 days. Within the splats, significant precipitation of the equilibrium Cr-rich second phase occurred. This phase appeared primarily in the largest splats, as the smaller splats suffered greater Cr loss to oxidation. The precipitate formed with an angular, blocky morphology that appeared to be preferentially oriented perpendicular to the splat edges.

Exposure up to 30 days generated further sintering of the structure and breakup of the oxide stringers into individual particles, Fig. 10(b). The Cr-rich phases were heterogeneously distributed through the coatings by this time. Two Cr-rich phases became apparent with extended exposure, based on their gray scale contrast. The darkest contrast Cr-rich phase was observed throughout the bulk of all of the coatings and had a very high Cr content



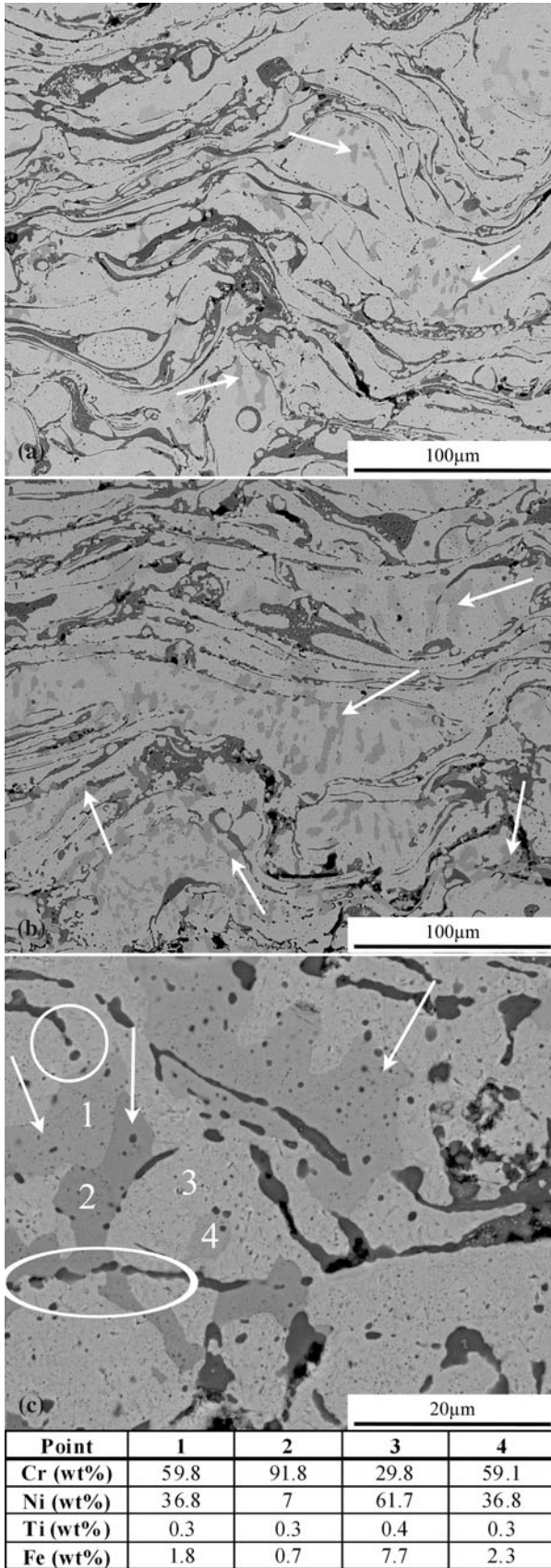
Point	1	2	3
Cr (wt%)	61.1	93	73.6
Ni (wt%)	36.5	4.1	23.3
Ti (wt%)	0.3	1.7	1.5

**Fig. 9** Cross-sectional BSE image of the oxidized surface of coating C after 5 days at 900 °C. The EDS analysis of the normalized Ni, Cr, and Ti compositions at Points 1-3 are shown in the table

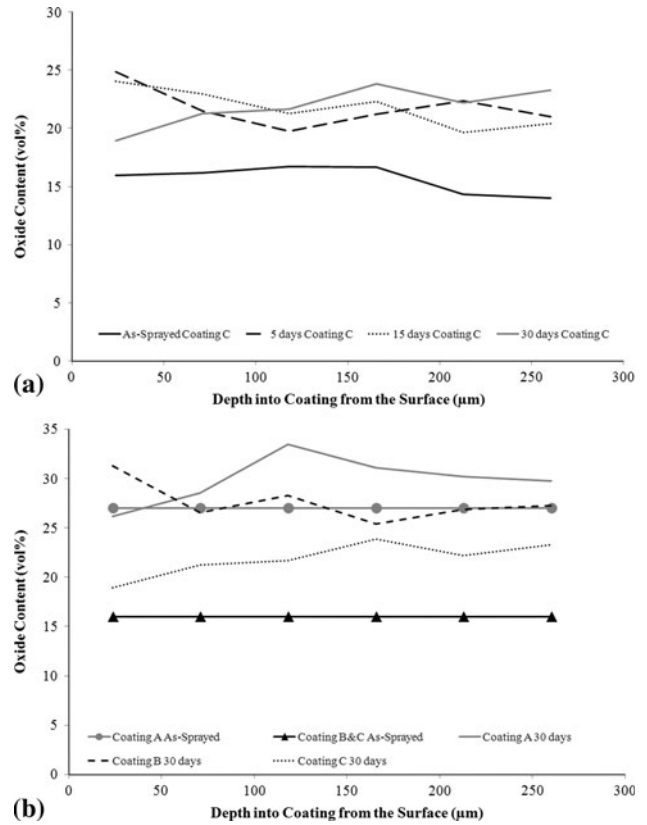
(>93 wt.%) as predicted from the Ni-Cr-Ti phase diagram (Ref 13). The lighter contrast Cr-rich phase was observed close to the substrate and had elevated levels of Ni (38-40 wt.%) and Fe (up to 2.5 wt.%). This high Ni content Cr-rich phase does not appear on the Ni-Cr-Ti phase diagram and is assumed to be a stable phase formed by the presence of Fe which diffused into the coating from the substrate. The responses of coatings A and B mirrored that of coating C and formed comparable microstructures after 30 days. All of the coatings were protective of the substrate over this time, with no significant oxide development was observed at the coating-substrate interface.

Figure 11 illustrates the extent of internal oxide development in coating C up to 30 days based on the “strip” analysis. Significant internal oxidation occurred within the first 5 days to a depth of 250 µm. No significant increase in the oxide content occurred after this time, supporting the conclusion that sintering and internal oxidation essentially sealed the coatings after 5 days. Coating C showed the lowest amount of internal oxidation, with coating A showing the highest. However, in comparison with the as-sprayed coatings, coatings B and C showed the greatest increase in oxide content, while coating A showed minimal oxide development. This is surprising given the more extensive surface oxide development on coating A in the topographical analysis. It is possible that the high concentration of oxide stringers within the coating offered some degree of corrosion protection to the splats, thereby minimizing the extent of oxide growth relative to the largely unoxidized coatings. If this is the case, then it has significant consequences for the effectiveness of the





◀**Fig. 10** Cross-sectional BSE images of coating C after 5 days (a) and 30 days (b) at 900 °C. The bottom image shows the variation in composition of the Cr-rich precipitate phases in the coating(c). The arrows highlight the Cr-rich precipitate phases. The circles highlight the spherical oxide features where the original plate-like oxide stringers have begun to break up into discrete spherical features with long-term high-temperature exposure



**Fig. 11** “Strip” analysis of the internal oxide content for coating C—as-sprayed condition and after 5, 15, and 30 days at 900 °C (a), and for the all of the coatings after 30 days at 900 °C (b)

coating as a corrosion barrier. While the internal oxides may minimize oxidation of the splats themselves, they would compromise the ability of the coating to seal itself by internal oxidation. This hypothesis was not resolved in this study, because, while the coating had a high as-sprayed oxide content, there was no significant oxidation of the substrate which indicated that the coating was protective.

EDS spot analysis within the cross section of several surface splats indicated that the extensive surface oxidation led to a significant reduction in the average Cr content of the surface splats over the first 5 days, beyond which the Cr content was stable, Fig. 12. Coatings B and C showed comparable Cr reductions from 42 to 29-32 wt.% after 30 days, while coating A suffered an average drop in Cr content of 27 wt.%.

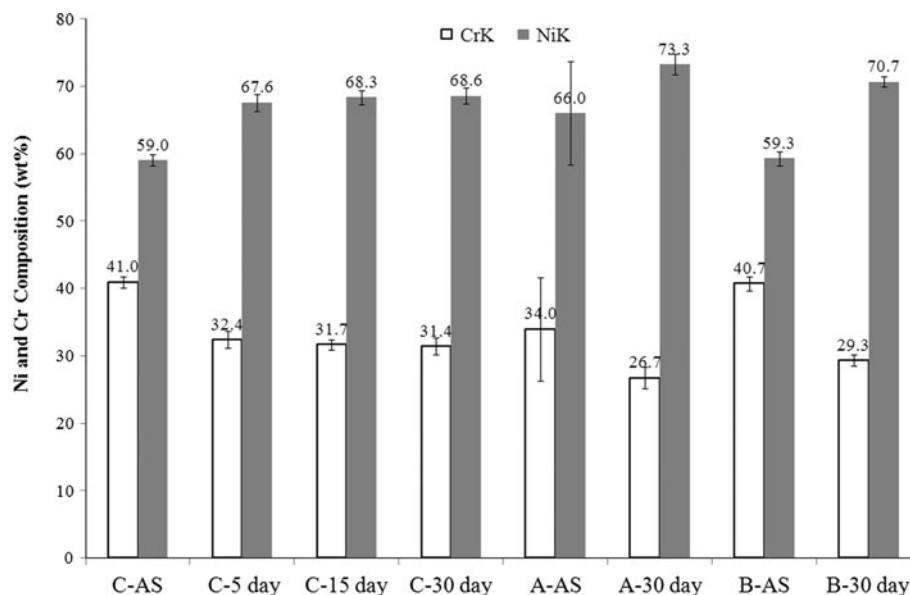


**Fig. 12** EDS spot analysis from the cross section of the surface splats showing the normalized Ni and Cr concentrations in coatings A (A), B (B), and C (C) in the as-sprayed condition (AS) and after exposure at 900 °C

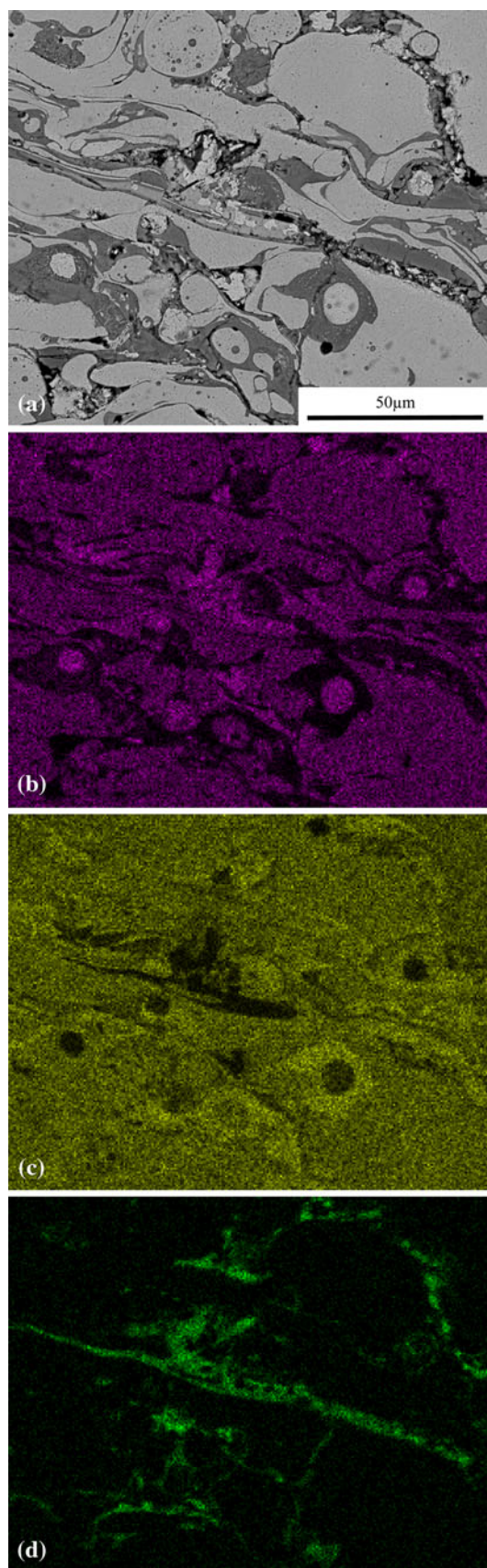
### 3.3 Smelt Deposit Corrosion

**3.3.1 Smelt Characterization.** XRD analysis indicated that the smelt powder was dominated by  $\text{Na}_2\text{S}\cdot(\text{H}_2\text{O})_5$  (JCPDS 01-084-0662) and  $\text{Na}_2\text{S}$  (JCPDS 23-441), with the lower intensity peaks of  $\text{Na}_2\text{SO}_4$  (JCPDS 01-074-1948). EDS analysis gave an average composition of Na: 76.4 wt.%, K 16.1 wt.%, S 5.4 wt.%, Cl 1 wt.%, and Ca 0.4 wt.%. This analysis did not include the low atomic mass elements, carbon or oxygen.

**3.3.2 Smelt Corrosion Testing: 400 °C.** Before XRD analysis, the layer of smelt was physically removed from the coatings to expose the corroded surfaces. This process may have removed some of the corrosion products with the smelt, but this was not investigated further. The XRD patterns for all of the coatings tested up to 30 days were dominated by the Ni alloy peaks of the coating, with minor peaks, indicating the presence of NiO and  $\text{Cr}_2\text{O}_3$ . No sulfur-based compounds or possible reaction products from the reaction of the smelt with the coating were identified. The presence of Ni and Cr oxides indicated that the test atmosphere had a significant oxygen partial pressure. It is thought that this allowed the coatings to form continuous oxide layers beneath the smelt deposit which impeded corrosion of the coatings. The test temperature was well below the melting point of industrial smelt (Ref 8), which limited corrosion to solid-state diffusion interactions between the smelt and oxidized coating. It is also probable that the main component of the smelt,  $\text{Na}_2\text{S}$ , was oxidized to  $\text{Na}_2\text{SO}_4$ . Unfortunately this would reduce the relevance of these results to corrosion in black liquor recovery boilers where the  $\text{Na}_2\text{S}$  would remain unoxidized because of the reducing conditions within the boiler. The presence of  $\text{Na}_2\text{SO}_4$  would shift the corrosion conditions to be more typical of those under so

called  $\text{Na}_2\text{SO}_4$  hot corrosion (Ref 7). This would explain the minimal corrosion observed, because hot corrosion only becomes significant upon the formation of a  $\text{Na}_2\text{SO}_4$  melt. The molten phase forms at the melting point of  $\text{Na}_2\text{SO}_4$  ( $T_{\text{MELT,Na}_2\text{SO}_4} = 884\text{ °C}$  (Ref 7)) under oxidizing conditions, or at lower temperatures under high partial pressures of  $\text{SO}_3$  in the gas phase (Ref 7). The low test temperature in this trial and lack of corrosive sulfur gases means that the deposit would have remained solid and prevented significant hot corrosion attack.

BSE cross-sectional images showed no corrosion of the coating. EDS area scans near the surface and near the substrate showed no variation in the sulfur content from background levels up to 30 days. Similarly there was no increase in corrosion products at the coating-substrate interface indicating that all three coating remained protective of the substrate under these test conditions. Within the coatings, the microstructure remained unchanged from their as-sprayed condition. The splat structures were still clearly evident, with no sign of splat sintering and the oxide morphologies appeared to be unchanged. EDS analysis of the oxides within coating A in the zone near the surface did not detect significant levels of sulfur, with the oxide compositions matching those in the as-sprayed condition. In contrast, the same internal oxide analysis in coating B showed a significant number of sulfur-rich features, Fig. 13. Their elemental composition typically showed high levels of Ni and Cr in addition to sulfur (the typical EDS sulfur content was 10-20 wt.%, with isolated spots as high as 35 wt.%). Considering that these oxide features already had high levels of Ni and Cr to begin with, it was not possible to definitively identify the composition of the sulfur compounds. The lack of Na or K at such sites meant that these were sulfur reaction products and not contamination from smelt. It was significant to



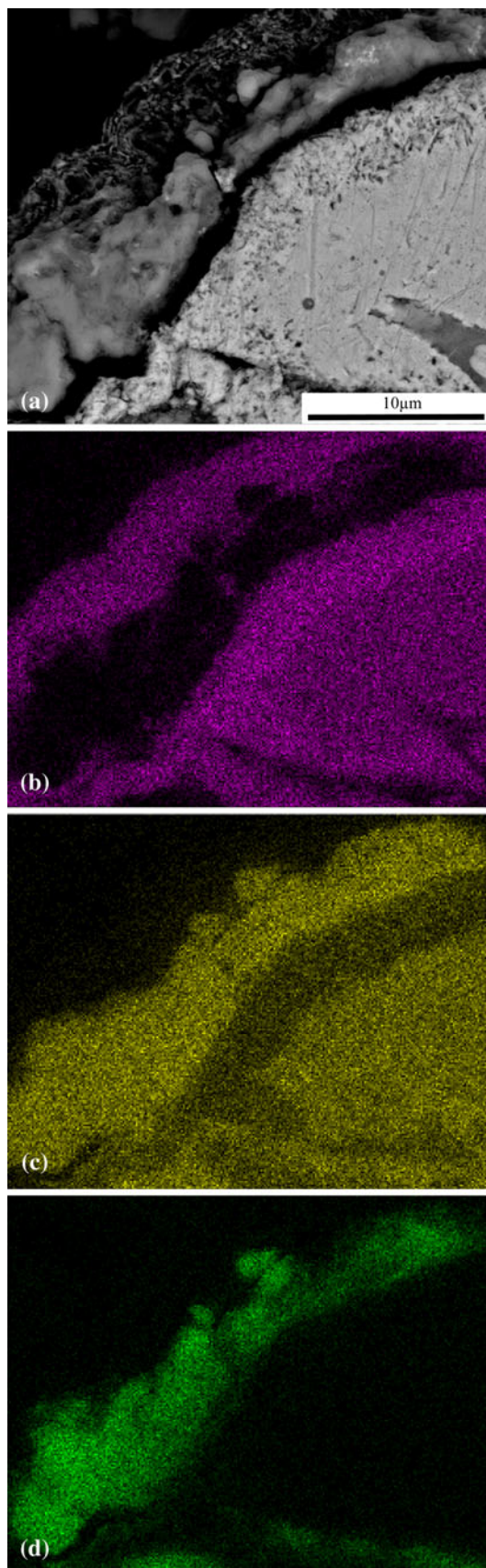
◀ **Fig. 13** Elemental mapping of the internal structure of coating B after 30 days at 400 °C under smelt, highlighting the penetration of sulfur along the splat boundaries—BSE image (a), Ni map (b), Cr map (c), and sulfur map (d)

note that such features were detected at depths in excess of 200 µm in the coating. The composition of the corrosive sulfur species and the mechanism by which it is penetrated the coating is unknown. Similar sulfur-rich features were seen within the internal oxide in the analysis of coating C. The significant variation in internal sulfidation between coating A and coatings B and C is thought to result from the high internal oxide content in coating A. Preformed Cr<sub>2</sub>O<sub>3</sub> oxide layers have been shown to protect or at least delay the onset of corrosion of chromia-forming alloys by sulfidation and hot corrosion (Ref 14-16). The oxide layers around each splat in coating A would inhibit reaction of the penetrating sulfur compounds with Cr from within the splat. While this would protect the individual splats from corroding, it would prevent the formation of chromium sulfides which are critical to sealing up the coating to prevent sulfur penetration to the substrate (Ref 1, 15, 17).

All of the coatings were observed to form sulfur compounds in the surface corrosion products. However, the thin nature and complex morphology of the corrosion products made it difficult to define the individual corrosion product compositions and morphologies. Chromium and sulfur-rich compounds were typically observed at the coating-oxide interface beneath outer Ni and Cr oxide layers, Fig. 14. Nickel and sulfur-rich compounds were typically observed in the outer part of the corrosion layers.

**3.3.3 Smelt Corrosion Testing: 800 °C.** After 30-day treatment at 800 °C, all of the coatings showed significant Ni oxide and Cr oxide formations in the XRD analysis, but no development of sulfur-rich corrosion products. This result again indicates a high oxygen partial pressure in the test atmosphere, which presumably also oxidized the smelt to Na<sub>2</sub>SO<sub>4</sub>. This hypothesis is supported by the fact that after 30 days, the original smelt deposit had a similar appearance to that in the 400 °C trials with no obvious signs of having formed a molten phase. Under industrial conditions, smelt is molten at this test temperature (Ref 8), while Na<sub>2</sub>SO<sub>4</sub> is still solid (Ref 7), indicating that some change in the smelt's composition probably occurred during testing. The solid state of the corrosive deposit, combined with the significant oxide formation on the coating accounts for the high corrosion resistance of the coatings under these conditions.

EDS area scans of the coating cross sections near the surface and substrate showed negligible variations in sulfur content, indicating minimal penetration of sulfur into the coating. The BSE cross section showed the formation of surface corrosion products but no obvious attack of the coatings. The coatings remained protective of the substrate in all cases. Within the coatings, there were obvious signs of splat sintering to form a bulk continuous Ni alloy material. The internal oxide composition mirrored that of the as-sprayed coating with only one analysis



◀ **Fig. 14** Elemental mapping of the surface corrosion product formed on coating B after 30 days at 400 °C under smelt, highlighting the formation of a (Cr+S)-rich phase—BSE image (a), Ni map (b), Cr map (c), and sulfur map (d)

spot indicating the presence of sulfur across all of the coatings. The oxide morphology showed signs of break up and spheroidization as noted at 900 °C. Precipitation of the Cr-rich second phase was also apparent in all coatings after 30 days.

### 3.4 Coating-Substrate Interdiffusion

Ni-Cr-Ti arc-sprayed coatings in industrial black liquor recovery boilers are expected to operate for many years, with only routine maintenance to repair localized corroded areas. The long-operating periods at high temperature enable interdiffusion between the coating and substrate to occur (Ref 18-20). EDS line scans were used to characterize the Fe, Ni, and Cr elemental profiles from the substrate into the coating, Fig. 15. Figure 15(a) shows the raw data plot for the three elements in coating C after 30 days at 900 °C. In the coating, the elemental distribution showed marked variability as the analysis line passed over Ni-rich splats and Cr-rich oxides. To better understand the interdiffusion in the coating alloy material, the following graphs show smoothed lines based on a manual interpretation of the normalized alloy composition in the coating.

The as-sprayed coatings showed vertical transitions in elemental concentration while moving from the substrate to the coating, indicating no interdiffusion occurring at the micron level of analysis. Similarly, there was no significant interdiffusion after 30 days at 550 °C, Fig. 15(b) and (c). In contrast, significant diffusion of Fe into the coating and Ni into the substrate occurred in all the coatings after 30 days at 800 °C, Fig. 15(b) and (c). The Cr profile showed a sharp spike in concentration at the coating-substrate interface, but no increase in the substrate Cr content with treatment up to 30 days. At 900 °C, Fe diffusion into the substrate developed up to 15 days to approximately 150 µm in coating C, with only minor variations up to 30 days, Fig. 15(f). Significant Ni counterdiffusion into the substrate occurred within the first 5 days, but did not develop significantly with extended exposure, Fig. 15(e). The Cr profile again showed a spike at the coating-substrate interface but no significant diffusion into the substrate, Fig. 15(d). After 30 days, all of the coatings showed comparable elemental profiles, particularly the depth of Fe diffusion into the coating.

Sundararajan et al. (Ref 19, 20) observed similar countercurrent diffusion between Ni-Cr coatings and a 9Cr-1Mo ferritic steel substrate during 1000-h steam oxidation trials at temperatures up to 750 °C. For Ni-20Cr coatings, they observed an increase in Fe diffusion into the coating and Ni diffusion into the substrate with increasing temperature (Ref 19). However, for the Ni-50Cr coatings, an increase in the temperatures from 600 to 750 °C led to a reduction in countercurrent diffusion of Fe and Ni

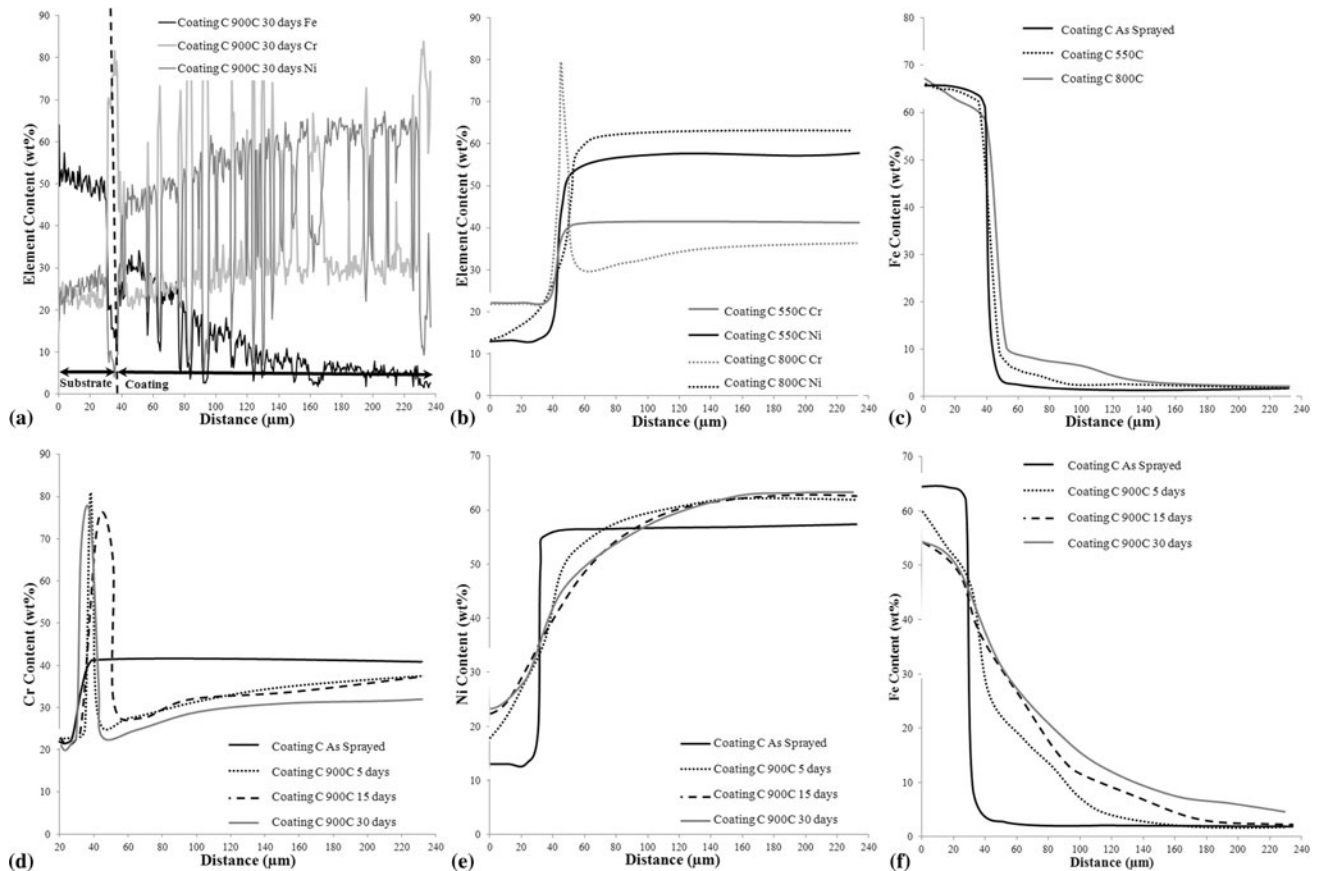


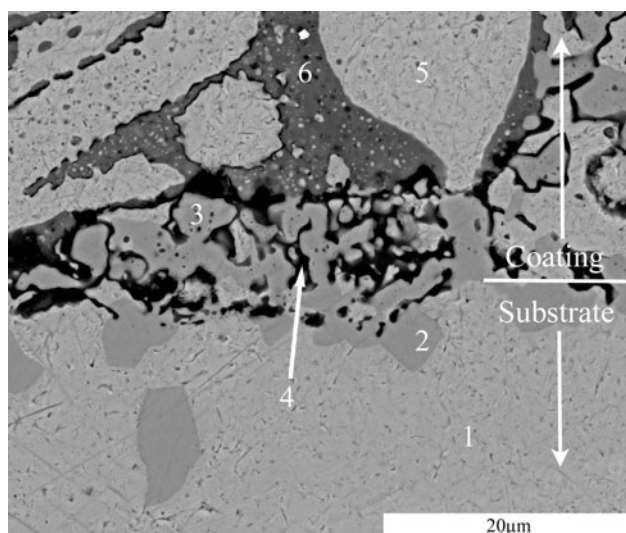
**Fig. 15** EDS elemental line scans showing the elemental distribution across the substrate-coating interface as a function of temperature. The scans start in the substrate (left side) and move into the coating (right)—raw data scan (a), Cr, Ni, and Fe scans for the coating C as-sprayed and after 30 days at 550 and 800 °C (b and c), and after exposure at 900 °C (d, e, and f)

(Ref 20). In both trials, no Cr diffusion into the substrate occurred, but there was noticeable enrichment of Cr at the coating-substrate interface. The diffusion coefficient for Cr and Ni in Fe are comparable (Ref 19), and Cr has been shown to readily diffuse from a Cr-rich/Fe-poor Ni alloy into a Cr-poor/Fe-rich Ni alloy in Ref 21. Sundararajan attributed the lack of Cr diffusion into the substrate to the reaction of Cr from the coating with carbon from the substrate to form chromium carbides at the interface (Ref 19). The rapid formation of these interface carbides with increasing temperature was postulated to account for the reduction in countercurrent diffusion with the increasing temperature in the Ni-50Cr coatings (Ref 20).

The lack of Cr diffusion into the substrate in this study was caused not by chromium carbides but by the formation of a Cr-rich metallic phase at the interface, Fig. 16. The gray scale contrast of this phase was comparable to those of the Cr-rich precipitates in the coating, indicating that it was of a similar atomic mass, while low oxygen and carbon peaks in the EDS spectrum indicated that this was not an oxide or carbide phase. The drop in the Cr/Ni ratio within the coating near the substrate interface indicated that Cr diffused from the coating into the substrate, which led to the precipitation of the Cr-rich phase predicted by the Fe-Cr-Ni ternary phase diagram for high Cr concentrations

(Ref 22). The interfacial region also showed elevated level of silicon, particularly within the dark contrast oxide phases, Fig. 16. It is postulated that Si from the substrate reacted with  $\text{Cr}_2\text{O}_3$  oxide stringers in the coating near the substrate interface, to reduce the  $\text{Cr}_2\text{O}_3$  to Cr while forming  $\text{SiO}_2$ . This mechanism may have contributed to the elevated Cr levels in this zone. The Cr-rich precipitates created a diffusion barrier to subsequent Cr diffusion into the substrate. They may have also reduced the extent of Fe diffusion into the coating with long-term exposure, as the rate of Fe diffusion in Cr is significantly less than in Ni (Ref 19).

Countercurrent diffusion of Fe and Ni into the coating and substrate occurs by lattice diffusion, which implies that sufficient splat sintering had occurred to form metallurgical bonding. This has important implications for the coating corrosion resistance, as the key pathway for penetration of corrosive species into the coating is along splat boundaries. If sufficient splat sintering occurs to allow Fe diffusion, then this implies that the splats at the coating surface will also undergo sintering and effectively seal the coating. This was seen in the cross-sectional analysis at both 800 and 900 °C. From this point, the coating effectively acts as a bulk body, with internal oxidation limited to the time it takes for splat sintering to occur. An additional benefit of



Point	1	2	3	4	5	6
Ni (wt%)	30.0	5.0	5.3	9.8	53.1	2.3
Cr (wt%)	20.5	79.9	82.3	44.0	22.4	91.3
Ti (wt%)	0.5	0.1	0.15	0.3	0.1	5.3
Fe (wt%)	47.8	14.8	11.5	14.8	23.6	0.9
Si (wt%)	2.1	0.2	0.8	31.2	0.8	0.1

**Fig. 16** Cross-sectional BSE image of the coating-substrate interface for coating A oxidized for 30 days at 900 °C, highlighting the formation of the Cr-rich phase in the substrate (Points 2 and 3)

forming a bulk body by sintering is that Cr from zones deeper within the coating can diffuse to the coating surface thus helping to maintain a protective oxide layer over a longer period of time.

Conversely, a lack of Fe diffusion implies minimal sintering of the splats and substrate has occurred. Therefore, the splat microstructure remains the dominant pathway for corrosive species to penetrate the coating. Corrosion prevention is then dependent on the oxidation of the splat surfaces to form bulk oxides to act as diffusion barriers to the ingress of corrosive species. The effectiveness of this approach is dependent on the concentration and oxidation rate of the oxide-forming elements in the splats and the splat morphology in terms of the “free path to substrate” defined in Ref 4. High oxide concentrations in the as-sprayed coatings are expected to inhibit this mechanism because of a reduction in oxide-forming elements in the alloy and the presence of oxide stringers which act as diffusion barriers to splat oxidation. Similarly, porous structures require greater degrees of oxide formation to seal the coating through internal oxidation relative to dense coating microstructures. These effects are particularly significant at low temperatures where Cr diffusion is slow, and hence,  $\text{Cr}_2\text{O}_3$  production to seal the coating takes a long period of time and only thin oxide layers are formed.

Applying this discussion to the results of this study would suggest that coatings A and B should be less corrosion resistant than coating C on account of their higher-oxide

content and porosity, respectively. These effects should have been the most significant in the low-temperature trials, since the Fe diffusion results indicated rapid sintering, and presumably sealing of all the coatings at higher temperatures. These effects were evident to a degree, with the high porosity of coating B leading to higher oxidative mass gain at 550 °C, and the high oxide content in coating A minimizing the extent of internal oxidation. However, in all cases, the coatings remained protective of the substrate. This indicates that under the conditions of this study (coating thickness, test duration, and exposure conditions) the variation in coating properties was insufficient to clearly show their effect on the coating corrosion protection of the substrate.

## 4. Conclusions

This study investigated the effect of coating microstructure on the corrosion performance of Ni-Cr-Ti arc-sprayed coatings under oxidizing conditions at 550 and 900 °C, and in an argon atmosphere, under smelt deposits at 400 and 800 °C. Three coatings’ microstructures were considered:

- A dense, oxidized coating (coating A) with an oxide content of 28.4 vol.% and a low, retained Cr content of 34 wt. %
- A porous coating with low oxide content (coating B) with a porosity of 5.3 vol.% and a high, retained Cr content of 40 wt. %
- An “optimized” coating (coating C) with a low porosity (3.5 vol.%) and a low oxide content (18.7%) and a high, retained Cr content of 40 wt. %

The key conclusions from this study are as follows:

- Coating porosity played a significant role in the oxidative mass gain, with coating B showing the highest mass gain at both 550 and 900 °C. Coatings A and C showed comparable weight gain results.
- In-flight oxidation significantly reduced the coating Cr content in coating A. During oxidation trials at 550 and 900 °C, this led to higher concentrations of NiO and  $\text{NiCr}_2\text{O}_4$  formed on this coating relative to those with higher, retained Cr contents.
- Internal oxidation occurred in all coatings at 550 and 900 °C. While coating A had the highest internal oxide content, this value showed only a minimal increase during oxidation testing. Coatings B and C showed greater increases in oxide content, with coating B consistently showing the largest increase because of its higher level of porosity.
- In spite of the variation in coating’s oxidation response, all of the coatings remained protective of the substrate during testing at 550 and 900 °C up to 30 days.
- No significant corrosion of the coatings occurred under the smelt deposits at 400 and 800 °C with the

30-day exposure time. This was attributed to oxidation of the coatings and the unmolten nature of the smelt in this study, which is at variance with the conditions experienced within industrial boilers. At 400 °C, sulfur penetrated the coating along the splat boundaries to depths exceeding 200 µm in coatings B and C. No sulfidation was observed in coating A because of the higher oxide content. At 800 °C, oxidation of the coatings formed protective oxide layers which prevented corrosion of the coating. A contributing factor was the possible oxidation of the smelt deposit which may have changed the composition from Na<sub>2</sub>S to Na<sub>2</sub>SO<sub>4</sub>. Sodium sulfate does not melt at the temperatures used in this study, which may have contributed to the lack of significant coating corrosion.

- Interdiffusion between the coating and substrate occurred at 800 and 900 °C, but no interdiffusion occurred at the lower temperatures. Significant diffusion of Fe occurred into the coating, while Ni was seen to diffuse from the coating into the substrate. Negligible Cr diffusion into the substrate occurred because of the formation of a Cr-rich metallic phase in the substrate which acted as a diffusion barrier.

## Acknowledgments

The authors gratefully acknowledge the support of Holster Engineering Company by supplying the wire and spraying the samples for this study. We would also like to thank Warren Blakemore for providing the smelt samples for this study and for his insight on the operation of industrial black liquor recovery boilers. The support provided by Professor Margaret Hyland in facilitating this study is gratefully appreciated.

## References

1. R. Luding, R. Thorpe, and R.V. Hinckley, The Development of Twin Wire Arc and HP/HVOF Sprayed Coatings for Coal-Fired Steam Generation Boiler, *Adv. Mater. Processes*, 2010, **168**(2), p 34-36
2. W. Zanchuk, The Use of Tafaloy 45CT, an Ni-Cr-Ti Alloy as an Arc Sprayed Corrosion Barrier in High Temperature Sulfurous Environments, *Surf. Coat. Technol.*, 1989, **39**(40), p 65-69
3. S. Matthews and M. Schweizer, Optimization of Arc-Sprayed Ni-Cr-Ti Coatings for High Temperature Corrosion Applications, *J. Therm. Spray Technol.*, this issue, 2013
4. S.T. Bluni and A.R. Marder, Effects of Thermal Spray Coating Composition and Microstructure on Coating Response and Substrate Protection at High Temperatures, *Corrosion*, 1996, **52**(3), p 213-218
5. K.R. Luer, J.N. DuPont, and A.R. Marder, High Temperature Sulfidation of Fe<sub>3</sub>Al Thermal Spray Coatings at 600 °C, *Corrosion*, 2000, **56**(2), p 189-198
6. M.A. Uusitalo, P.M.J. Vuoristo, and T.A. Mantyla, High Temperature Corrosion of Coatings and Boiler Steels in Oxidising Chlorine-Containing Atmosphere, *Mater. Sci. Eng. A*, 2003, **346**, p 168-177
7. N. Birks, G. Meier, and F. Pettit, *High Temperature Oxidation of Metals*, Cambridge University Press, Cambridge, 2006
8. N. Otsuka, Fireside Corrosion, *Shreir's Corrosion (Part IV: High Temperature Corrosion Environments)*, T. Richardson, Ed., Elsevier, Amsterdam, 2010, p 457-481
9. D. Young, High Temperature Oxidation and Corrosion of Metals, *Elsevier Corrosion Series*, T. Burstein, Ed., Elsevier, Amsterdam, 2008
10. S. Al-Hassan, P.M. Singh, and G.J. Fonder, Effect of Smelt/Gas Interaction on SA-210 Carbon Steel Corrosion, *Proceedings of the 1998 International Chemical Recovery Conference*, Institute of Paper Science and Technology, Atlanta, 1-4 June 1998, p 901-908
11. R.A. Peascoe, J.R. Keiser, J.G. Hemrick, M.P. Brady, P. Sachenko, C.R. Hubbard, R.D. Ott, C.A. Blue, and J.P. Gorog, Materials Issues in High Temperature Black Liquor Gasification, *TAPPI Fall Technical Conference*, Chicago, 2003, p 5037-5045
12. W.S. Rasband, ImageJ, US National Institute of Health, <http://imagej.nih.gov/ij/>, 1997-2012
13. N. Lebrun, Cr-Ni-Ti (Chromium-Nickel-Titanium), *Light Metal Ternary Systems: Phase Diagrams, Crystallographic and Thermodynamic Data*, G. Effenberg and S. Ilyenko, Ed., Springer, Berlin, 2008
14. G. Romeo and D.W. McKee, The Na<sub>2</sub>SO<sub>4</sub>-Induced Corrosion Properties of Ni-Base Superalloy Phases, *J. Electrochem. Soc.*, 1975, **122**(2), p 188-199
15. M.F. Stroosnijder and W.J. Quadackers, A Corrosion Study of Ni and Ni-Cr Alloys in SO<sub>2</sub>/H<sub>2</sub>O/H<sub>2</sub> Atmospheres Using Gas Analysis, *Corros. Sci.*, 1989, **29**(9), p 1059-1072
16. X.G. Zheng and D.J. Young, Sulphide Formation After Pre-oxidation of Chromia Formers, *Corros. Sci.*, 1996, **38**(11), p 1877-1897
17. D. Rezakhani, Corrosion Behaviours of Several Thermal Spray Coatings Used on Boiler Tubes at Elevated Temperatures, *Anti-Corros. Methods Mater.*, 2007, **54**(4), p 237-243
18. B. Singh and S. Prakash, Analytical Studies on the Behavior of Nickel and Cobalt-Base Shrouded Plasma Spray Coatings at Elevated Temperature in Air, *Oxid. Met.*, 2007, **67**, p 279-298
19. T. Sundararajan, S. Kuroda, T. Itagaki, and F. Abe, Steam Oxidation Resistance of Ni-Cr Thermal Spray Coatings on 9Cr-1Mo Steel: Part 1: 80Ni-20Cr, *ISIJ Int.*, 2003, **43**(1), p 95-103
20. T. Sundararajan, S. Kuroda, T. Itagaki, and F. Abe, Steam Oxidation Resistance of Ni-Cr Thermal Spray Coatings on 9Cr-1Mo Steel: Part 2: 50Ni-50Cr, *ISIJ Int.*, 2003, **43**(1), p 104-111
21. K.M. Day and M.A. Dayananda, Analysis of interdiffusion in selected high temperature alloy systems, *Heat Treating: Proceedings of the 23rd Heat Treating Society Conference*, D. Herring and R. Hill, Eds., ASM International, Materials Park, 2006, p 332-337
22. "Cr (Chromium) Ternary Alloy Phase Diagrams," *ASM Handbook, Volume 03—Alloy Phase Diagrams*, H. Baker and H. Okamoto, Eds., ASM International, Materials Park, 1992, p 3.42-43.49